


Photoluminescence Imaging and LBIC Characterization of Defects in mc-Si Solar Cells

L.A. SÁNCHEZ ^{1,2} A. MORETÓN,¹ M. GUADA,¹
S. RODRÍGUEZ-CONDE,¹ O. MARTÍNEZ,¹ M.A. GONZÁLEZ,¹
and J. JIMÉNEZ¹

1.—GdS-Optronlab, Dpto. Física de la Materia Condensada, Universidad de Valladolid, Edificio LUCIA, Paseo de Belén 19, 47011 Valladolid, Spain. 2.—e-mail: lasandom92@gmail.com

Today's photovoltaic market is dominated by multicrystalline silicon (mc-Si) based solar cells with around 70% of worldwide production. In order to improve the quality of the Si material, a proper characterization of the electrical activity in mc-Si solar cells is essential. A full-wafer characterization technique such as photoluminescence imaging (PLi) provides a fast inspection of the wafer defects, though at the expense of the spatial resolution. On the other hand, a study of the defects at a microscopic scale can be achieved through the light-beam induced current technique. The combination of these macroscopic and microscopic resolution techniques allows a detailed study of the electrical activity of defects in mc-Si solar cells. In this work, upgraded metallurgical-grade Si solar cells are studied using these two techniques.

Key words: Solar cells, multicrystalline silicon, UMG silicon, LBIC, photoluminescence

INTRODUCTION

Multicrystalline silicon (mc-Si) is the basis of the current photovoltaic (PV) market due to its low production cost and relatively high efficiency. Upgraded metallurgical-grade silicon (UMG Si) has been raised as an alternative to the traditional purification obtained by the Siemens process because of its reduced production cost and time.^{1,2} Although the Siemens process produces the purest material, solar cells fabricated with wafers from UMG Si have achieved efficiencies around 20%.³

UMG Si contains more impurities, such as shallow acceptors and donors, which reduce the carrier diffusion lengths and limit the cell efficiency.⁴ In order to improve the quality of UMG Si, it is essential to know the type of defects and the detrimental role played by the recombination centers for the photogenerated carriers. Photoluminescence imaging (PLi) and light-beam induced current (LBIC) techniques have proved to be powerful

characterization tools for measuring the electrical activity of defects in mc-Si solar cells.^{5–8} In PLi the sample is excited with optical radiation to emit luminescence, and a CCD camera is used to acquire the luminescence emission signal. This technique does not require electrical contacts and is applicable not only to solar cells, but also to bricks, as-cut wafers and processed wafers.⁹ PLi provides a macroscopic spatially-resolved image of the electrical activity of a solar cell in a short time, depending on the quantum efficiency of the camera. Silicon CCD cameras can detect only a very small portion of the Si band-to-band luminescence emission, usually requiring long exposure times. However, indium gallium arsenide (InGaAs) cameras are sensitive to the luminescence spectrum of Si, and operate at shorter exposure times than Si CCD cameras. Dark contrasted areas in the images obtained by PLi can be associated with grain boundaries, dislocations, micro-cracks, etc. In LBIC, a light source is focused and scanned point by point over a surface area of the solar cell, and the generated electron–hole pairs produce a current.¹⁰ This photocurrent is collected at each point of the selected area; its intensity

(Received November 24, 2017; accepted May 11, 2018)

depends on the recombination of minority carriers. LBIC images reveal the spatial distribution of the recombination centers. This technique, in contrast to PLi, allows a very high spatial resolution, but it is more time consuming than PLi. In this work we study defects in UMG mc-Si solar cells at macroscopic and microscopic scales using these two techniques.

EXPERIMENTAL

PL imaging was measured by the homemade setup represented schematically in Fig. 1a. The PLi excitation system contained four 20 W laser diodes (808 nm wavelength). The photoluminescence emission of the solar cell was captured in a dark environment with a 1392×1040 pixels Si CCD camera (PCO 1300 solar). In order to get a full image of the solar cell, a 12.5 mm focal length objective was coupled to the camera. A longpass filter with a cutoff wavelength of 900 nm was mounted in front of the camera to remove the background light. Alternatively, PL emission was also captured with an InGaAs camera (Hamamatsu C12741-03).

A homemade LBIC system was used to obtain highly detailed information about the defects in the solar cells. The scheme of the LBIC setup is shown in Fig. 1b. The LBIC apparatus consisted of four excitation wavelengths from two dual laser diodes (Omicron). The laser lines were 639 nm, 830 nm, 853 nm, and 975 nm, allowing us to achieve different penetrations depths. Here, only the 853 nm line was used. A beam-splitter divided the output beam of the laser (10 mW) into two beams. One of them was used to measure variations in the output power through a photodiode. The other one was directed into a trinocular microscope which focused the laser onto the solar cell. Different objectives ($20\times$, $50\times$, $100\times$) enabled studies up to a very high spatial resolution, circa $1 \mu\text{m}$ for the $100\times$ objective. A Si

CCD camera coupled to the top ocular was used to collect the light reflected by the sample and drive the auto-focus system through edge detection. The LBIC scanning was obtained by moving the sample in an x - y - z motorized translation stage (Prior Scientific) over areas as large as $76.7 \times 114.5 \text{ mm}^2$ and step sizes as small as $1 \mu\text{m}$. The generated photocarriers were collected by an electrometer (Keithley Instruments) and data acquisition and hardware control was developed in LabVIEW.

UMG mc-Si solar cells provided by Silicio Ferrosolar were characterized through the PLi and LBIC techniques. PLi was carried out on a total of 30 UMG mc-Si solar cells divided into three series. A-series cells have efficiencies ranging between 17.4% and 17.6%, B-series cells have efficiencies between 16.8% and 17.0% and C-series cells have efficiencies between 16.4% and 16.8%. LBIC measurements were carried out on one cell of each series.

RESULTS AND DISCUSSION

Figure 2a, b, and c shows the PL images obtained in three solar cells corresponding, respectively, to series A, B, and C. These images present dark areas that correspond to non-radiative recombination regions due to grain boundaries (GBs) and intra-grain defects, mainly dislocations. A first look to these images shows that the C-series solar cell image contains a greater number of dark areas. The three series of measured solar cells yielded different values of photoluminescence intensity signal. Higher values of cell efficiency produced higher values of PL intensity. This PL intensity signal is expressed in terms of the mean value of the intensity over all the pixels of the PL image. In order to obtain a valid relation between PL images the cells were characterized using the same parameters of exposure time, aperture and excitation power. It is also necessary that the solar cells were

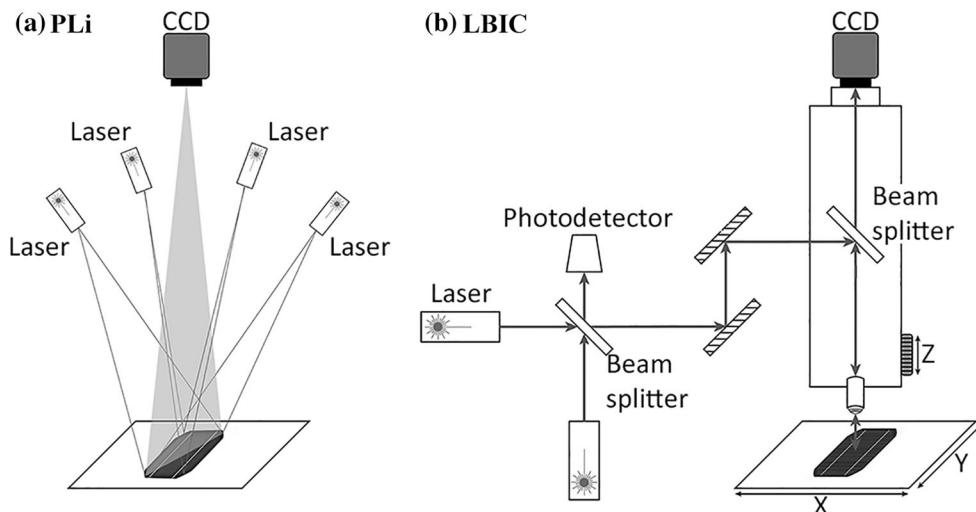


Fig. 1. (a) Scheme of the PLi system. (b) Scheme of the LBIC system.

manufactured using the same technology. An almost linear dependence is shown in Fig. 2d, where the maximum, minimum and mean values of this PL intensity signal are plotted for each solar cell series. Very similar results were found with the two cameras used in the experiment, the Si CCD camera and the InGaAs camera. The exposure times with the InGaAs camera were shorter because of its higher quantum efficiency in the silicon emission spectral window. In particular, the exposure time value used in the experiments was 150 ms for the InGaAs camera instead of the 30 s used for the Silicon CCD camera.

Figure 3a and b shows the PL image of a solar cell from the C-series, and the LBIC map of a highly defective zone obtained with a 20 \times objective. Whereas the PLi revealed a dark cloud because of the poor spatial resolution, the LBIC map allowed us to resolve the structure of the defect, which appears as an array of dark contrasted lines, resolved because of the higher spatial resolution of the LBIC setup. Most of these defects correspond to dislocations inside the grains. The LBIC contrast is significantly enhanced because of the large local variations of the photocurrent induced by the laser

beam. The LBIC map acquisition time was almost 24 h, but necessary to map this 18,000 \times 18,000 μm^2 region of the solar cell with a lateral resolution of 60 μm . More information about these defects can be obtained by improving the spatial resolution by using a higher magnification objective. Figure 3c shows a comparison between PLi (left) and LBIC (right) of the GBs in an area with a high concentration of metallic impurities. In PLi the GBs present a bright contrast that does not match with the expected high recombination activity. This is due to the low spatial resolution of the technique. The dark contrast associated to GBs can be appreciated along with the bright contrast that appears in PLi when the high spatial resolution of LBIC is used. The bright contrast around the GBs can be associated to depletion of impurities, as they tend to accumulate at the GBs due to the strains field during the solidification process.

Figure 4a, b, and c shows 400 \times 400 μm^2 LBIC maps of A, B, and C-series solar cells using a 100 \times objective. These measurements revealed a slightly bright contrasted line along the core of the defects in all the series. This local bright contrast is due to variations in the light reflectivity, as we will discuss

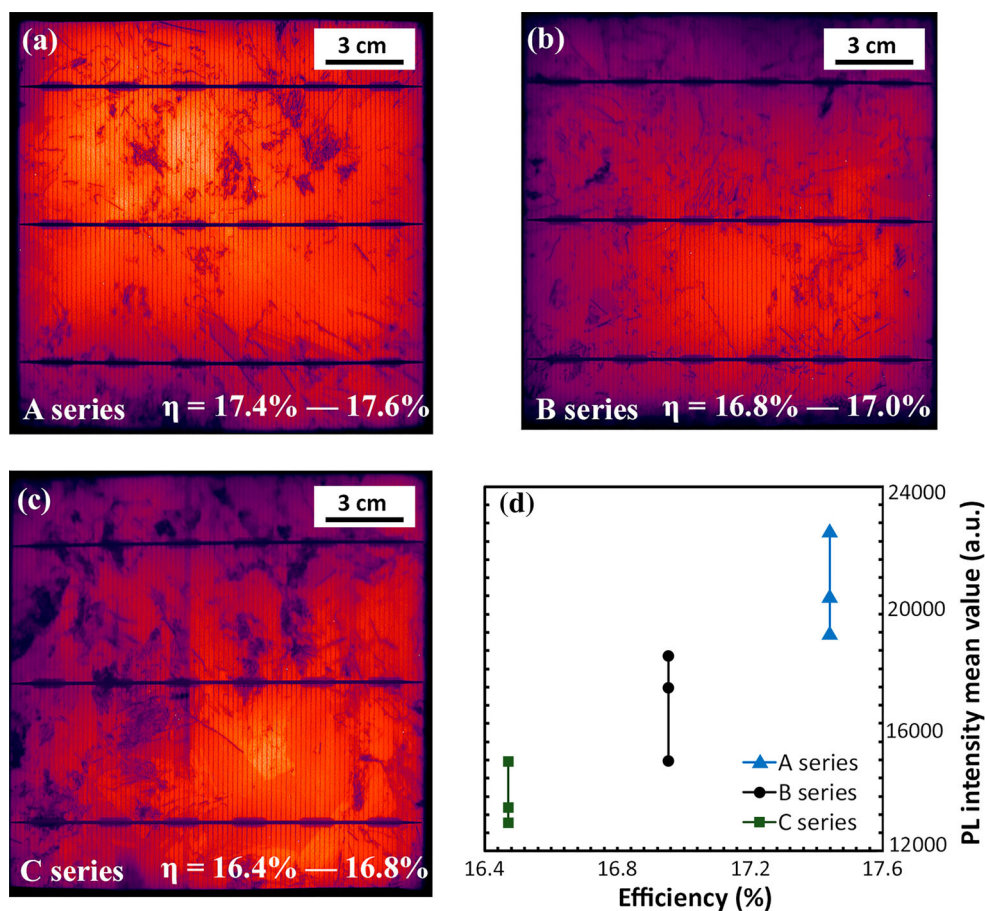


Fig. 2. (a)–(c) PL images of three solar cells of A, B, and C series. (d) The PL intensity signal obtained for each series increases with the efficiency.

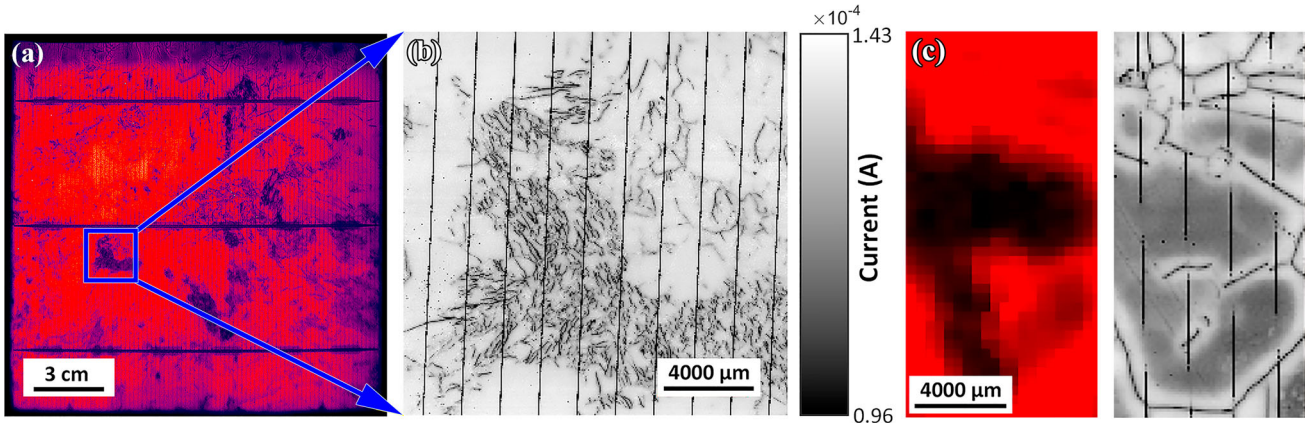


Fig. 3. (a) PL image of a C-series solar cell. (b) Corresponding LBIC map of the selected area in the PL image ($18,000 \times 18,000 \mu\text{m}^2$, $20\times$ objective, step size $60 \mu\text{m}$). (c) Comparison between PLi (left) and LBIC (right) of an area with high concentration of metallic impurities.

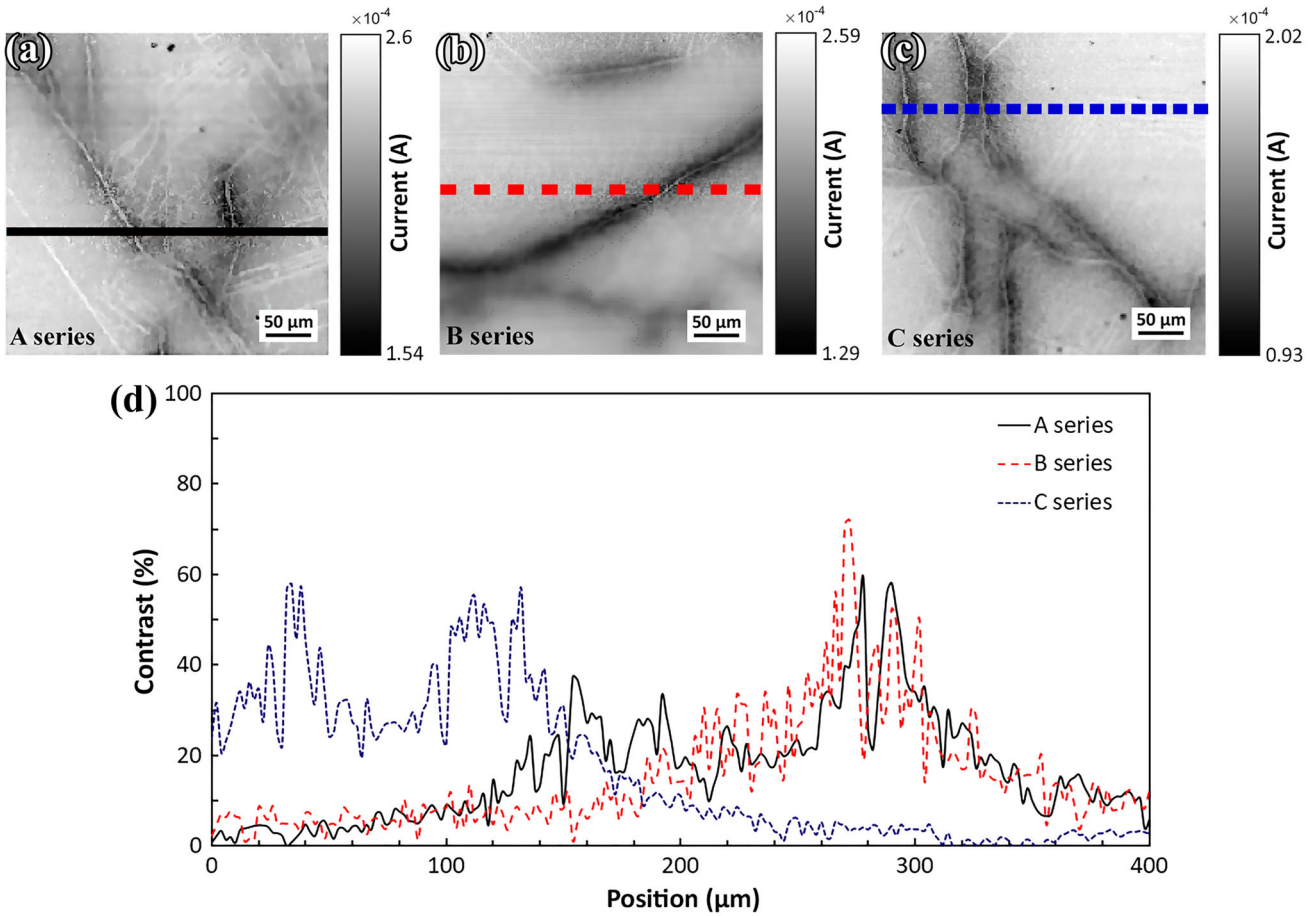


Fig. 4. (a)–(c) LBIC maps of defective areas in three solar cells of A, B, and C series ($400 \times 400 \mu\text{m}^2$, $100\times$ objective, step size $2 \mu\text{m}$). (d) Photocurrent contrast across the lines marked in this figure.

later. Figure 4d shows the LBIC contrast across the lines marked in Fig. 4a, b, and c. This LBIC contrast is defined by

$$C = (I_b - I_d)/I_d \quad (1)$$

where I_b is the background photocurrent measured in a defect-free region and I_d is the photocurrent measured in a defective region.¹¹ The contrast is essentially the same in the three solar cells near the defects, so the lower efficiencies in the B and C series can be explained not as an increase of the

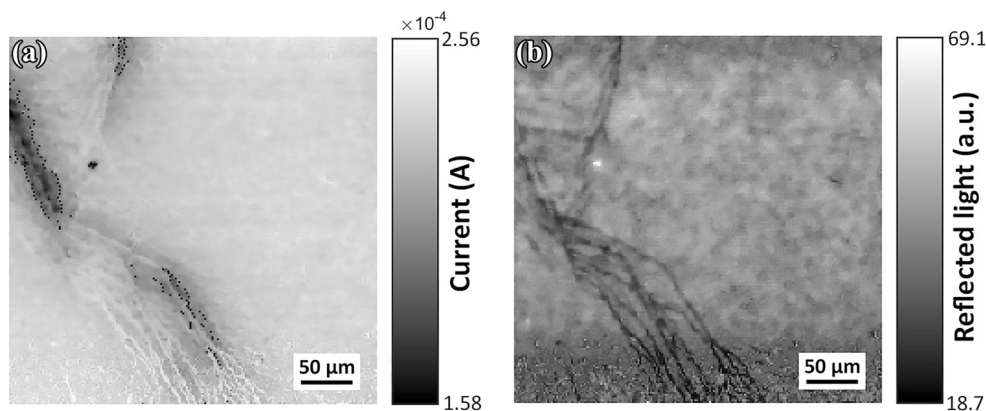


Fig. 5. (a) LBIC map of a C-series solar cell area presenting dark spots ($400 \times 400 \mu\text{m}^2$, $100\times$ objective, step size $2 \mu\text{m}$). (b) Corresponding reflected light map. Note the high LBIC signal in the regions with low reflectivity, see the array of dark contrasted lines in the reflectivity map and the bright contrast in the LBIC map, evidencing the importance of the reflectivity for the LBIC contrast.

electrical activity of the defects, but as the consequence of a greater density of defects.

Figure 5b shows the reflected light map of a C-series sample obtained with the Si-CCD camera coupled to the microscope. This map permits us to see low light reflectivity at the core of the dark defect lines. This suggests that the higher local photocurrent detected in the core of the defect lines can be associated with a higher light absorption at those zones with the concomitant increase of the associated photocurrent.

Some of the B and C-series solar cells presented tiny dark spots in some regions around the defects (Fig. 5a), with a pronounced drop in the photocurrent. Figure 5b shows the reflected light map of a C-series sample obtained with the Si-CCD camera coupled to the microscope. UMG Si contains more metallic impurities than traditional solar grade Si; therefore, these dark spots can be explained as an accumulation of metallic impurities. These impurities give rise to clusters without electrical activity, because there is no charge capture in their vicinity.¹² The reflected light map also showed low reflective regions without high capture rates around them in the corresponding LBIC measurement.

CONCLUSION

In this work, we studied the electrical activity of defects in several UMG mc-Si solar cells of known efficiencies through PLi and LBIC techniques. PLi allowed a fast full-wafer observation of the cells, with a good correlation between the mean value of PL intensity signal and the solar cell efficiencies. A detailed description of the defective areas revealed by PLi was achieved by high spatial resolution LBIC mapping. In summary, we have shown the complementarity between the low spatial resolution PLi

technique and the high spatial resolution LBIC images. While the PLi technique allows a fast qualification of the cells, a profound analysis of the defects demands the high resolution of the LBIC technique. Furthermore, both techniques must be combined with the acquisition of the reflected light images in order to better understand the origin of the contrast in both images. Future studies will focus on the role of the impurities on the electrical activity of grain boundaries and intragrain defects using UMG Si cells, because of the high concentration of residual impurities in this material, compared to materials produced by the traditional Si purification method.

ACKNOWLEDGEMENTS

This work was supported by the Spanish MINECO Project, ref. ENE2014-56069-C4-4-R and “Junta de Castilla y León (Spain)” Project Number VA081U16. We thank Silicio Ferrosolar for providing the samples studied in this work.

REFERENCES

1. N. Yuge, M. Abe, K. Hanazawa, H. Baba, N. Nakamura, Y. Kato, Y. Sakaguchi, S. Hiwasa, and F. Aratani, *Prog. Photovolt. Res. Appl.* 9, 203 (2001).
2. D. Kohler, B. Raabe, S. Braun, S. Seren, and G. Hahn, in *Proceedings of the 24th European Photovoltaic Solar Energy Conference* (2009), pp. 1758–1761.
3. F. Rougieux, C. Samundsett, K.C. Fong, A. Fell, P. Zheng, D. Macdonald, J. Degouange, R. Einhaus, and M. Forster, *Prog. Photovolt. Res. Appl.* 24, 725 (2016).
4. M. Forster, P. Wagner, J. Degouange, R. Einhaus, G. Galbiati, F. Rougieux, A. Cuevas, and E. Fourmond, *Sol. Energy Mater. Sol. Cells* 120, 390 (2014).
5. T. Trupke, B. Mitchell, J.W. Weber, W. McMillan, R.A. Bardos, and R. Kroeze, *Energy Procedia* 15, 135 (2012).
6. M. Bliss, X. Wu, K. Bedrich, T. Betts, R. Gottschalg, and I.E.T. Ren, *Pow. Gener.* 9, 446 (2014).

7. B. Moralejo, M.A. González, J. Jiménez, V. Parra, O. Martínez, J. Gutiérrez, and O. Charro, *J. Electron. Mater.* 39, 663 (2010).
8. M.K. Juhl, M.D. Abbot, and T. Trupke, *IEEE J. Photovolt.* 7, 1074 (2017).
9. B. Moralejo, A. Tejero, O. Martínez, M.A. González, J. Jiménez, and V. Parra, in *Proceedings of the 2013 Spanish Conference on Electron Devices* (2013), pp. 353–356.
10. B. Moralejo, V. Hortelano, M.A. González, O. Martínez, J. Jiménez, S. Ponce-Alcántara, and V. Parra, *Phys. Status Solidi (c)* 8, 1330 (2011).
11. S. Binetti, M. Acciarri, and J. Libal, *Solid State Phenom.* 131–133, 419 (2008).
12. J. Chen, B. Chen, W. Lee, M. Fukuzawa, M. Yamada, and T. Sekiguchi, *Solid State Phenom.* 156–158, 19 (2010).